Bubble dynamics and sonoluminescence from helium or xenon in mercury and water

Kyuichi Yasui* and Kazumi Kato
National Institute of Advanced Industrial Science and Technology (AIST), 2266-98 Anagahora, Shimoshidami, Moriyama-ku, Nagoya 463-8560, Japan

(Received 7 May 2012; revised manuscript received 3 September 2012; published 26 September 2012)

Numerical simulations of bubble pulsation and sonoluminescence (SL) have been performed for helium or xenon bubbles in mercury and water under the experimental conditions of Futakawa *et al.* [M. Futakawa, T. Naoe, and M. Kawai, in *Nonlinear Acoustics—Fundamentals and Applications: 18th International Symposium on Nonlinear Acoustics (ISNA 18)*, AIP Conf. Proc. No. 1022, edited by B. O. Enflo, C. M. Hedberg, and L. Kari (AIP, New York, 2008), p. 197]. The results of the numerical simulations have revealed that the bubble expansion is much larger in water than in mercury mainly because the density of water is one order of magnitude smaller than that of mercury. The SL intensity is higher in water than that in mercury although the maximum bubble temperature is lower. This is caused by the much larger amount of vapor inside a bubble as the saturated vapor pressure of water is four orders of magnitude larger than that of mercury at room temperature. The SL intensity from xenon is much larger than that from helium due both to lower ionization potential and higher bubble temperature due to lower thermal conductivity. The instantaneous SL power may be as large as 200 W from xenon in water. The maximum temperature inside a xenon bubble in mercury may be as high as about 80 000 K. It is suggested that the maximum pressure in mercury due to shock waves emitted from bubbles increases as the SL intensity increases, although they are not simply correlated in water because the amount of water vapor trapped inside a bubble influences the SL intensity in a complex way.

DOI: 10.1103/PhysRevE.86.036320 PACS number(s): 47.55.dd, 78.60.Mq, 43.25.+y

I. INTRODUCTION

Neutron scattering is a useful method in condensed matter physics to investigate the lattice structure of especially light atoms such as oxygen and hydrogen because the scattering cross section does not increase with atomic number, in contrast to x rays [1–5]. Furthermore, thermal neutrons of about 25 meV in kinetic energy have a de Broglie wavelength of about 0.18 nm which is in the same order of magnitude as atomic spacing in condensed matter. As the energy (∼25 meV) is comparable to the intermolecular energies in condensed phases, thermal neutrons are a powerful tool for the investigation of dynamical and geometrical properties of matter. In addition, as a neutron has a magnetic dipole moment without electric charge, neutron scattering can be used in the study of magnetic materials. Thus, neutron scattering has been widely used in studies of liquids, glasses, amorphous materials, biomaterials, polymers, foods, membranes, etc.

There are mainly two types of neutron sources [1,6]. One is a nuclear fission reactor in which a nuclear chain reaction takes place ($^{235}\mathrm{U} + n \rightarrow \mathrm{A} + \mathrm{B} + 2.3\ n$, where A and B are fission fragments). The other is a spallation source in which target atoms (mercury) are fragmented by a high energy proton beam from an accelerator ($p + \mathrm{Hg} \rightarrow \mathrm{A} + \mathrm{B} + xn$). Although the spallation reaction takes place in all elements, mercury is currently mostly used in spallation sources because the liquid metal itself is a good coolant when high power proton beams are penetrated into the target, and there is not much radiation damage compared to the solid target as well as the high neutron yield [7,8].

There is, however, a difficult problem in the mercury target [7–14]. In the spallation sources, a pulsed (25–60 Hz) high energy (1–3 GeV) proton beam penetrates into the liquid metal with the beam power of up to 1–5 MW to produce high neutron fluxes. The duration of each pulse is very short ($<1\ \mu$s) and the temperature rise of the affected volume is not so high (∼10 °C). Nevertheless, the extreme local heating rate (on the order of 10^7 °C/s) may cause the propagation of high intensity pressure waves in the liquid metal. When the pressure wave is reflected at the container's surface, the local pressure instantaneously becomes negative, which causes cavitation in the liquid metal. Cavitation is the appearance and subsequent collapse of bubbles. When the cavitation bubbles collapse near the container's surface, microjets as well as micro shock waves hit the surface. It causes the cavitation damage of the surface of the liquid container. It is a severe problem because the service lifetime of the container is extremely shortened.

In order to study the behavior of cavitation bubbles in mercury, Futakawa and his co-workers [15–18] have studied bubble dynamics as well as the light emission from collapsing bubbles called sonoluminescence (SL) in mercury. In the experimental system, the cavitation event is produced by imposing mechanical impacts onto the shallow stainless-steel cylinder filled with mercury (not degassed) using the disk plate specimen driven with the striker controlled by the electromagnetic force that is determined by the input electric power. The input electric power was kept constant (560 W) at which the morphology of the cavitation damage was similar to that observed in the actual proton beam experiments [15]. Under the condition, the light emission (SL) from the bubbles was observed by a photomultiplier tube through the transparent glass window fixed on the lid of the chamber [15].

SL in mercury was experimentally observed by Kuttruff in 1962 [19]. The optical spectrum of SL from cavitation driven by an acoustic wave in mercury showed a strong continuum. Smith *et al.* [20] reported SL from liquid metals such as Hg,

*k.yasui@aist.go.jp

Ga, In, Sn, and Bi at 20 °C above each melting point. The brightest SL among the liquid metals studied by them was mercury.

The bubble dynamics in mercury has been numerically studied by Ida and his co-workers [16–18,21]. However, in their studies, effects of nonequilibrium evaporation and condensation of mercury vapor, ionization of vapor and gas molecules, and the light emission were completely neglected. In the present paper, we have performed numerical simulations of bubble dynamics and SL taking these effects into account.

II. MODEL

The present model has been described in Refs. [22–24]. A part of the model has been validated from studies of single-bubble SL which is the light emission from a single stable bubble trapped at the pressure antinode of a standing ultrasonic wave [25]. The other part of the model on the bubble-bubble interaction for a multibubble system has also been validated from studies of cavitation bubbles under an ultrasonic horn [26].

When there are many bubbles in the liquid, as in the case of cavitation in mercury in the experiment of Futakawa *et al.* [15], it is necessary to take into account the effect of the bubble-bubble interaction in the calculations of the bubble pulsation [22,26,27]. The bubble-bubble interaction is the influence of acoustic waves radiated by surrounding bubbles on the pulsation of a bubble. When we assume that the equilibrium radii of the bubbles are the same and that the spatial distribution of the bubbles is uniform, then this complex problem is simplified as Eq. (1):

$$\begin{aligned}&\left(1-\frac{\dot R}{c}+\frac{\dot m}{c\rho_{L,i}}\right)R\ddot R+\frac{3}{2}\dot R^2\left(1-\frac{\dot R}{3c}+\frac{2\dot m}{3c\rho_{L,i}}\right)\\&=\frac{1}{\rho_{L,\infty}}\left(1+\frac{\dot R}{c}\right)[p_B-p_a(t)-p_0]\\&\quad+\frac{\ddot m R}{\rho_{L,i}}\left(1-\frac{\dot R}{c}+\frac{\dot m}{c\rho_{L,i}}\right)+\frac{\dot m}{\rho_{L,i}}\\&\quad\times\left(\dot R+\frac{\dot m}{2\rho_{L,i}}+\frac{\dot m\dot R}{2c\rho_{L,i}}-\frac{R}{\rho_{L,i}}\frac{d\rho_{L,i}}{dt}-\frac{\dot m R}{c\rho_{L,i}^2}\frac{d\rho_{L,i}}{dt}\right)\\&\quad+\frac{R}{c\rho_{L,\infty}}\frac{dp_B}{dt}-S(R^2\ddot R+2R\dot R^2),\end{aligned}\tag{1}$$

where R is the instantaneous bubble radius, $\dot R=\frac{dR}{dt}$, t is time, c is the sound velocity in the liquid near the bubble wall, $\dot m$ is the rate of evaporation of liquid at the bubble wall (negative value means condensation), $\rho_{L,i}$ is the liquid density at the bubble wall, $\ddot R=\frac{d^2R}{dt^2}$, $\rho_{L,\infty}$ is the liquid density far from a bubble, p_B is the liquid pressure at the bubble wall, $p_a(t)$ is the instantaneous applied pressure at time t, p_0 is the ambient static pressure, $\ddot m=\frac{d\dot m}{dt}$, and S is the coupling strength of a bubble cloud introduced in Refs. [22,26,27] as follows:

$$\begin{aligned}S=\sum_i\frac{1}{d_i}&=\int_{l_{\min}}^{l_{\max}}\frac{4\pi r^2n}{r}dr=2\pi n\left(l_{\max}^2-l_{\min}^2\right)\\&\approx 2\pi nl_{\max}^2,\end{aligned}\tag{2}$$

TABLE I. The van der Waals constants of gas and vapor inside a bubble [30].

	a (10^{-1} J m^3/mol^2)	b (10^{-5} m^3/mol)
He	0.0346	2.38
Xe	4.19	5.16
Hg	5.19	1.06
H_2O	5.54	3.05

where d_i is the distance between the bubble and another bubble i, the summation is for all the bubbles, n is the number density of bubbles, $l_{\max}$ is the radius of the bubble cloud in which bubbles are assumed to be homogeneously distributed, $l_{\min}$ is the distance between a bubble and the nearest bubble, and $l_{\max}\gg l_{\min}$ has been assumed in the last equation. The last term of Eq. (1) represents the effect of the bubble-bubble interaction.

It has been theoretically indicated that the bubble wall velocity ($\dot R$) never exceeds the sound velocity in the liquid near the bubble wall (c) [28]. Thus, in the present numerical simulations, when $|\dot R|$ exceeds c during the bubble collapse ($\dot R<-c$), $|\dot R|$ is replaced by c ($\dot R=-c$). For water, c is calculated as a function of pressure at the bubble wall (p_B) as follows: $c=\sqrt{7.15(p_B+B)/\rho_{L,i}}$, where $B=3.049\times10^8$ Pa [29]. For mercury, $c=1450$ m/s is assumed.

The liquid pressure at the bubble wall (p_B) is related to the pressure inside a bubble (p) as follows:

$$p_B=p-\frac{2\sigma}{R}-\frac{4\mu}{R}\left(\dot R-\frac{\dot m}{\rho_{L,i}}\right)-\dot m^2\left(\frac{1}{\rho_{L,i}}-\frac{1}{\rho_{in}}\right),\tag{3}$$

where σ is the surface tension, μ is the liquid viscosity, and ρ_{in} is the density inside a bubble. The pressure inside a bubble (p) is estimated by the van der Waals equation of state:

$$\left(p+\frac{a}{v^2}\right)(v-b)=R_gT,\tag{4}$$

where a and b are the van der Waals constants, v is the molar volume of gas and vapor inside a bubble, R_g is the gas constant (=8.3145 J/mol K), and T is the temperature inside a bubble. The van der Waals constants for gases and vapor are listed in Table I [30].

The pressure (P) of acoustic waves radiated from bubbles in the bubble cloud is expressed by the following equation using the coupling strength (S) [31]:

$$P=S\rho_{L,\infty}(R^2\ddot R+2R\dot R^2).\tag{5}$$

TABLE II. Physical property of mercury and water at normal condition [30].

	Mercury	Water
Density (g/cm^3)	13.5	1.0
Saturated vapor pressure (Pa)	0.2	2300
Surface tension (N/m)	0.48	0.073
Sound speed (m/s)	1450	1480
Viscosity (10^{-3} Pa s)	1.56	1.00
Heat capacity [J/(kg K)]	140	4200
Thermal conductivity [W/(m K)]	8	0.6

The physical properties of mercury and water at normal conditions are listed in Table II [30]. In the present numerical simulations, the liquid temperature at the bubble wall is calculated as a function of time using the model described in Refs. [24,32]. Thus, the saturated vapor pressure is calculated as a function of the liquid temperature using the formula described in Refs. [32,33] for water and in Ref. [34] for mercury. The thermal conductivity of the liquid is also calculated as a function of temperature by the formula in Ref. [35] for water and by interpolating the experimental data [36] for mercury.

The temperature inside a bubble is calculated as follows. The temperature (T) is related to the thermal energy (E) of a bubble as Eq. (6):

$$E = nC_V T - \frac{an^2}{V}, \tag{6}$$

where n is the number of molecules inside a bubble in moles, C_V is the molar specific heat of gas and vapor inside a bubble, a is the van der Waals constant, and V is the bubble volume. The temporal change in the thermal energy is calculated by Eq. (7):

$$\Delta E = -p\Delta V + 4\pi R^2 \kappa_T \left.\frac{\partial T}{\partial r}\right|_{r=R} \Delta t + 4\pi R^2 e\dot{m}\Delta t + \Delta H - \Delta H_{\rm ion} + \left[-\frac{3}{5} M\dot{R}\ddot{R}\right]\Delta t, \tag{7}$$

where ΔE is the change of the thermal energy in a short time Δt, p is the pressure inside a bubble, ΔV is the change in the bubble volume, κ_T is the thermal conductivity of gas and vapor inside a bubble, $\frac{\partial T}{\partial r}|_{r=R}$ is the temperature gradient at the bubble wall, e is the energy carried by evaporating or condensing vapor molecules per unit mass, ΔH is the heat of chemical reactions which is absent in mercury, $\Delta H_{\rm ion}$ is the heat of ionization of gas and vapor molecules inside a bubble, and M is the total mass of the gases and vapor inside a bubble. The last term of Eq. (7) is the change in the macroscopic kinetic energy of gas and vapor inside a bubble that is transferred into heat. The term is included only when the term is positive. The thermal conductivity (κ_T) of gas and vapor is estimated as a function of temperature as listed in Table III [37,38].

The number (n) of molecules inside a bubble changes with time due to nonequilibrium evaporation or condensation at the bubble wall. The rate of evaporation ($\dot{m}$) at the bubble wall is calculated as follows:

$$\dot{m} = \dot{m}_{\rm eva} - \dot{m}_{\rm con}, \tag{8}$$

$$\dot{m}_{\rm eva} = \frac{\alpha_M p_v^*}{\sqrt{2\pi R_v T_{L,i}}}, \tag{9}$$

$$\dot{m}_{\rm con} = \frac{\alpha_M \Gamma p_v}{\sqrt{2\pi R_v T_B}}, \tag{10}$$

TABLE III. Thermal conductivity (κ_T) of gas and vapor inside a bubble [W/(m K)] assumed in the present numerical simulations as a function of temperature (T in K) [37,38]. For Hg (MW = 201), the experimental data for Rn (MW = 199–226) are used.

He	$2.4 \times 10^{-4} T + 7.8 \times 10^{-2}$
Xe	$1.5 \times 10^{-5} T + 1.3 \times 10^{-3}$
Hg	$1.1 \times 10^{-5} T - 7.2 \times 10^{-4}$
H_2O	$1.0 \times 10^{-4} T - 1.2 \times 10^{-2}$

where $\dot{m}_{\rm eva}$ ($\dot{m}_{\rm con}$) is the actual rate of evaporation (condensation), α_M is the accommodation coefficient for evaporation and condensation, p_v^* is the saturated vapor pressure, R_v is the gas constant of vapor in J/(kg K), $T_{L,i}$ is the liquid temperature at the bubble wall, Γ is the correction factor, p_v is the partial pressure of vapor inside a bubble, and T_B is the temperature of gas and vapor at the bubble wall. In the present model, $T_{L,i}$ and T_B are different due to the presence of the temperature jump at the bubble wall. For water, the accommodation coefficient (α_M) decreases from 0.35 to 0.05 as the liquid temperature at the bubble wall increases from 350 to 500 K according to the molecular dynamics simulation by Matsumoto [24,39]. For mercury, α_M is assumed as 1.

In the present study, the diffusion of gas across the bubble wall is taken into account although it is negligible under the present condition [40,41]:

$$\frac{dN_{\rm diff}}{dt} = -4\pi R^2 D \frac{A}{B} \frac{c_i - c_\infty}{(R_0/R)^2 R_0}, \tag{11}$$

where $dN_{\rm diff}/dt$ is the number of gas molecules flowing into the bubble per unit time, D is the diffusion coefficient of the gas in the liquid, $A = \langle (R/R_0) \rangle$, $B = \langle (R/R_0)^4 \rangle$, $\langle\rangle$ denotes the time averaged value, R_0 is the ambient bubble radius which is defined as the bubble radius when an acoustic wave is absent, c_i is the concentration of the gas near the bubble surface, and c_∞ is the concentration far from a bubble. The gas diffusion rate is proportional to the bubble surface area ($4\pi R^2$) and the gradient of gas concentration in the liquid near the bubble wall. The concentration gradient is inversely proportional to $(R_0/R)^2$ because the thickness of a constant material volume becomes smaller as a bubble expands, which is called the shell effect [42].

The model for the ionization of the gas and vapor molecules has been described in Ref. [23]. The ionization potentials of gas and vapor molecules in vacuum are listed in Table IV [30]. In the present model, the reduction in ionization potential by the high density inside a bubble has been taken into account as follows [23,28,43,44]. The reduction is caused by the overlap of the electron wave functions of gas and vapor molecules. Thus, the reduced ionization potential ($\chi_{\rm red}$) is estimated by Eq. (12):

$$\chi_{\rm red} = \chi \left(1 - \frac{1}{y}\right), \tag{12}$$

TABLE IV. The ionization potential of gas and vapor in vacuum in eV.

He	24.6
Xe	12.1
Hg	10.4
Hg^+	18.8
H_2O	12.6
OH	13.0
H_2	15.4
H	13.6
O	13.6
O_2	12.1

where χ is the ionization potential in vacuum (Table IV),

$$y = \frac{1}{2a_B k'} \sqrt[3]{\frac{V}{n_t}}, \tag{13}$$

where a_B is the Bohr radius (5.29×10^{-11} m), $k\prime$ is the ratio of the radius of the gas molecule to that of a hydrogen atom, V is the bubble volume, and n_t is the total number of molecules inside a bubble. The reduction in ionization potential inside SL bubbles has been experimentally suggested [45]. For mercury, the ionization of Hg^+ is also taken into account.

The model for the light emission has been described in Refs. [23,28]. The light emission processes taken into account in the model are electron-atom bremsstrahlung, electron-ion bremsstrahlung, radiative recombination of electrons and ions, radiative attachment of electrons to neutral atoms and molecules, and chemiluminescence of OH. Electron-atom bremsstrahlung is the light emission from free electrons accelerated by the collisions with neutral atoms and molecules during their thermal motion, which has been regarded as the main source of SL emission in water [23,46,47]. As the optical spectrum of SL in mercury showed a strong continuum according to Kuttruff [19], the line emissions from Hg are neglected in the present study.

The amplitude of a distortion of the spherical bubble surface is also calculated as a function of time. A small distortion of the spherical surface is described by $R + a_n Y_n(\theta,\phi)$, where R is the mean radius of a bubble, a_n is the distortion amplitude, $Y_n(\theta,\phi)$ is a spherical harmonic of degree n, and θ, ϕ are angles in the polar coordinates. The dynamics for the distortion amplitude a_n is given by the following equation [40,48]:

$$\ddot{a}_n + B_n(t)\dot{a}_n - A_n(t)a_n = 0, \tag{14}$$

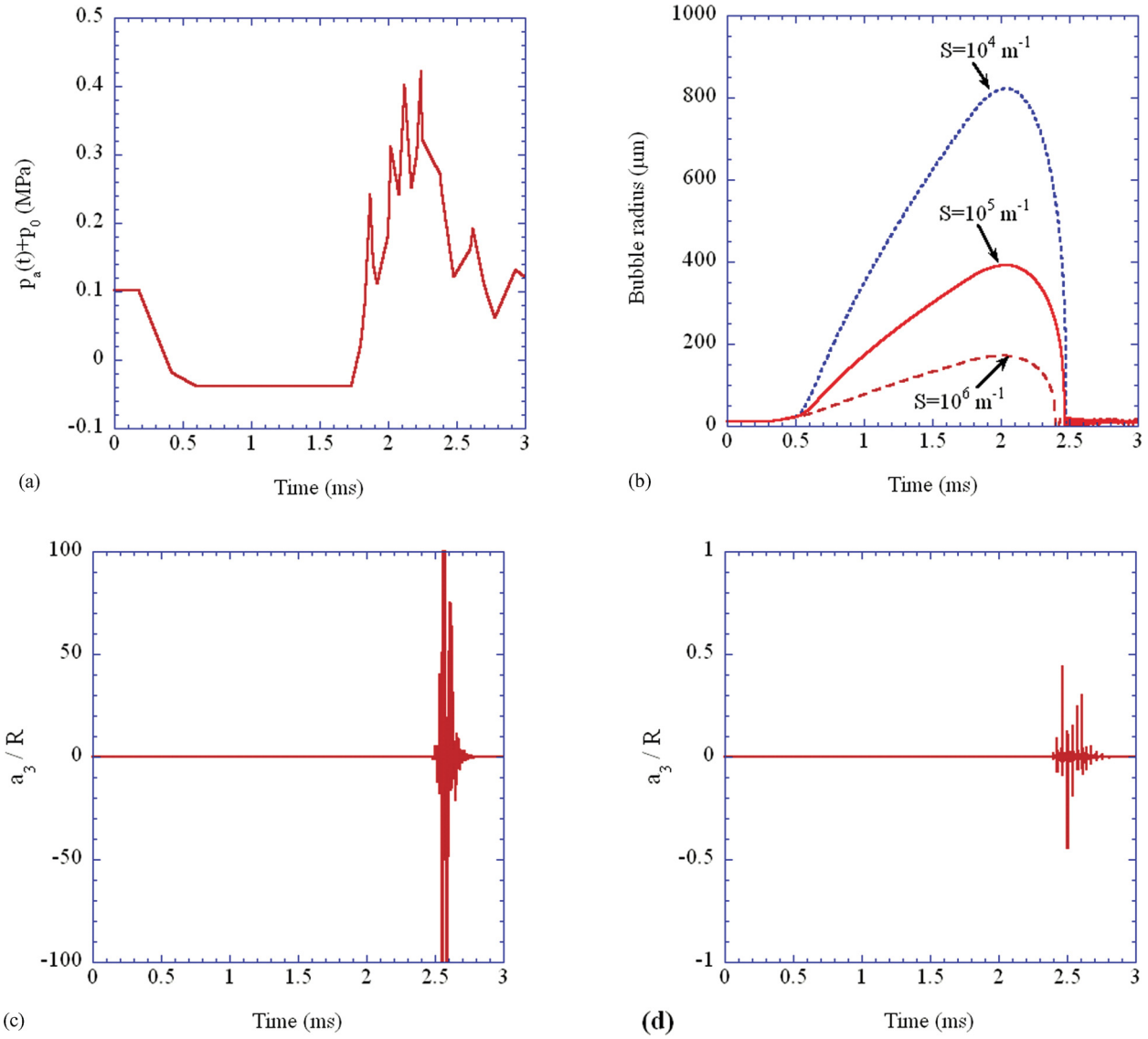

FIG. 1. (Color online) The result of numerical simulations as a function of time for 3 ms. (a) The applied pressure plus the ambient static pressure assumed in the simulations. (b) The radius of a He bubble in mercury for various values of S. The initial bubble radius (R_0) is 10 μm. (c) The distortion amplitude of the mode $n = 3$ relative to the instantaneous bubble radius for $S = 10^5$ m^{-1}. (d) Sames as in (c), but for $S = 10^6$ m^{-1}.

where the overdot denotes the time derivative (d/dt),

$$A_n(t) = (n-1)\frac{\ddot{R}}{R} - \frac{\beta_n \sigma}{\rho R^3} - \left[(n-1)(n+2) + 2n(n+2)(n-1)\frac{\delta}{R}\right]\frac{2\mu\dot{R}}{R^3}, \quad (15)$$

and

$$B_n(t) = \frac{3\dot{R}}{R} + \left[(n+2)(2n+1) - 2n(n+2)^2\frac{\delta}{R}\right]\frac{2\mu}{R^2}, \quad (16)$$

where $\beta_n = (n-1)(n+1)(n+2)$, σ is the surface tension, μ is the liquid viscosity, and δ is the thickness of the thin layer where fluid flows,

$$\delta = \min\left(\sqrt{\frac{\mu}{\omega}}, \frac{R}{2n}\right), \quad (17)$$

where ω is the angular frequency of ultrasound.

III. RESULTS AND DISCUSSIONS

In the experiment of Futakawa *et al.* [15], a cavitation experiment was performed for mercury in which helium was dissolved. Thus, in the present paper, we will first discuss dynamics and sonoluminescence of helium bubbles. In Fig. 1(b), the bubble radius is shown as a function of time for various values of S when the temporal pressure variation $[p_a(t) + p_0]$ is given by Fig. 1(a) as experimentally measured by Futakawa *et al.* [15]. As expected from the previous studies [22,26,27], the bubble expansion is strongly suppressed by the bubble-bubble interaction and the maximum bubble radius decreases as S increases. The initial bubble radius (R_0) is assumed as 10 μm because a bubble does not sufficiently expand to emit light for $R_0 \leqslant 9$ μm as has already been pointed out by Ida *et al.* [16,17]. For $S = 10^4$ and 10^5 m^{-1}, a bubble disintegrates into daughter bubbles just after the violent bubble collapse and the second collapse, respectively, because the distortion amplitude exceeds the mean bubble radius [a_3/R exceeds 1 in Fig. 1(c) for $S = 10^5$ m^{-1}]. For $S = 10^5$ (10^4) m^{-1}, the distortion amplitude of the mode $n = 3$ ($n = 6$) is the largest. On the other hand, for $S = 10^6$ m^{-1}, a bubble is shape stable and never disintegrates into daughter bubbles because the bubble collapse is milder compared to the cases of $S = 10^4$ and 10^5 m^{-1} and the distortion amplitude is always smaller than the mean bubble radius [Fig. 1(d)]. For this case, the distortion amplitude of the mode $n = 3$ is the largest. For all the cases, bubbles experience the violent collapse and shape instability takes place only after the violent collapse.

The temperature inside a bubble dramatically increases at the end of the bubble collapse as seen in Fig. 2 for helium bubbles in mercury with $S = 10^5$ m^{-1}. The maximum temperature is about 10 000 K [Fig. 2(a)]. The number of mercury atoms inside a bubble is more than four orders of magnitude smaller than that of helium atoms due to the very small saturated vapor pressure of mercury [Fig. 2(b)]. Although the ionization potential of helium is reduced by about 44% due to the high pressure inside a bubble at the end of the bubble collapse, the degree of ionization of helium atoms is only 10^{-4}. On the other hand, the degree of ionization

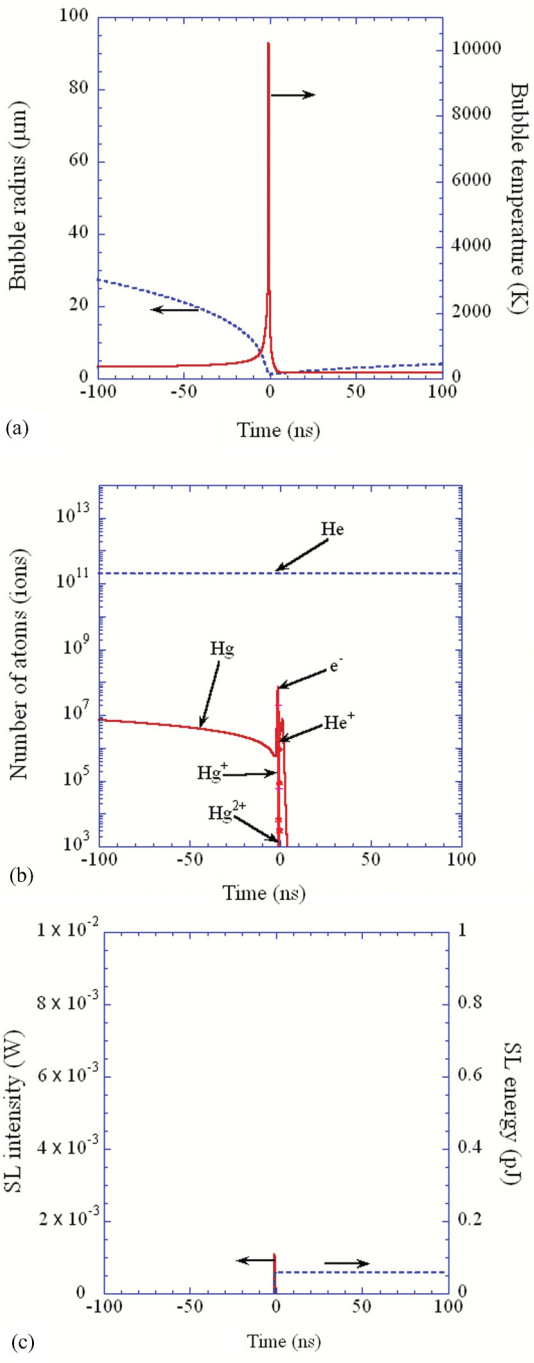

FIG. 2. (Color online) The result of the numerical simulation for a He bubble in mercury as a function of time for 200 ns near the end of the bubble collapse ($R_0 = 10$ μm, $S = 10^5$ m^{-1}). (a) The bubble radius (dotted line) and the temperature inside a bubble (solid line). (b) The number of atoms (ions) inside a bubble with the logarithmic vertical axis. (c) The SL intensity (solid line) and its time integral (dotted line).

of mercury vapor is as high as about 0.2 because the ionization potential is much lower than that of helium. In the present case, the number of free electrons is about three orders of magnitude smaller than the total number of atoms inside a bubble at the end of the bubble collapse. Nevertheless, the SL intensity of a few milliwatts is comparable to that of normal single-bubble

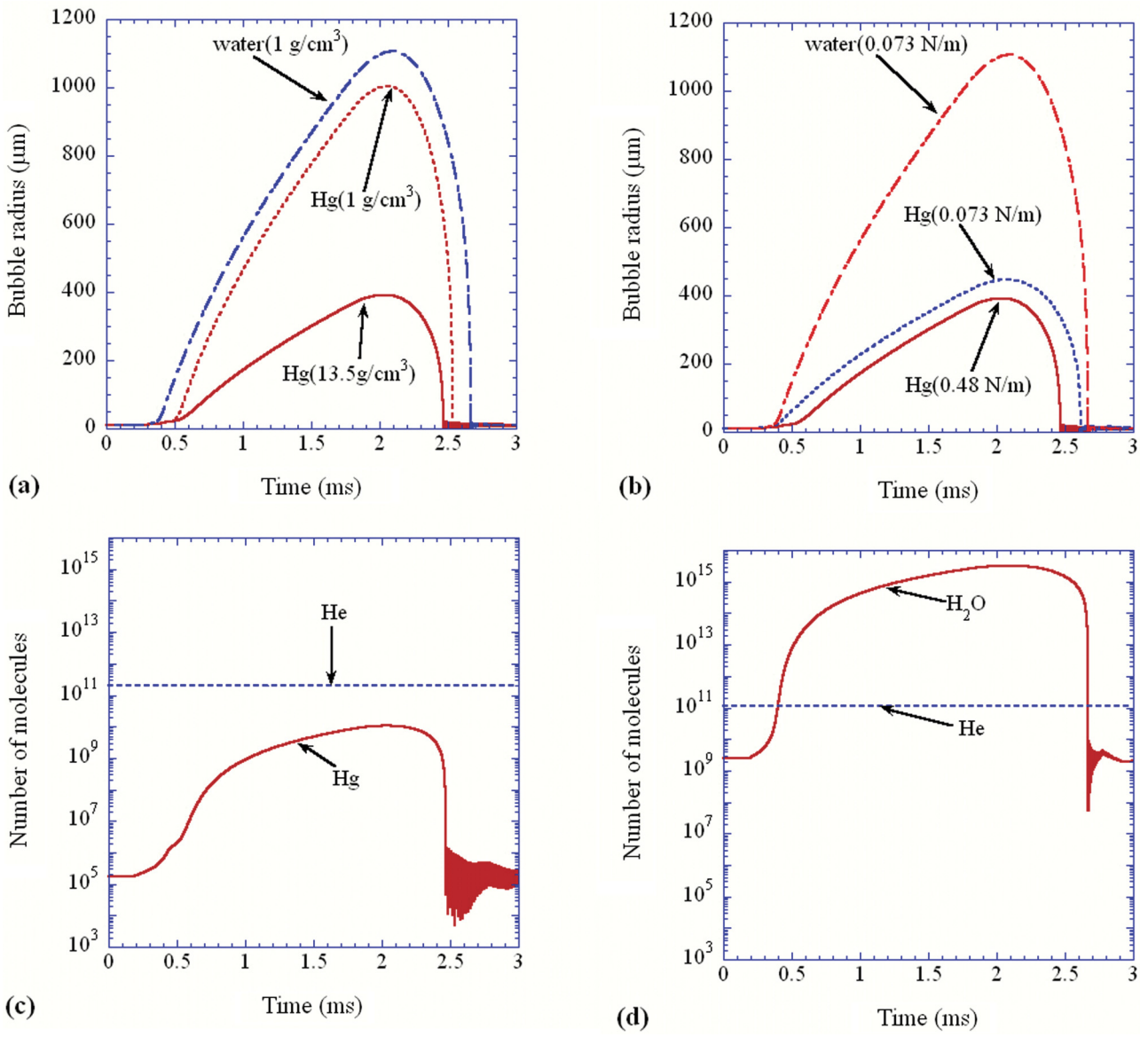

FIG. 3. (Color online) The comparison between the result of the numerical simulation for He bubbles in water and that in mercury as a function of time for 3 ms ($R_0 = 10$ μm, $S = 10^5$ m^{-1}). (a) The bubble radius in water, mercury, and imaginary mercury with the density of water. (b) The bubble radius in water, mercury, and imaginary mercury with the surface tension of water. (c) The number of molecules inside a bubble in mercury with the logarithmic vertical axis. (d) Sames as in (c), but in water.

sonoluminescence (SBSL) in water under ultrasound due to a larger equilibrium radius (10 μm) of a bubble compared to that for SBSL (about 5 μm) [47,49,50].

Now we discuss the difference in bubble dynamics between mercury and water. A bubble expands much more in water than in mercury mostly due to the smaller density of water [Fig. 3(a)]. A bubble in water disintegrates into daughter bubbles just after the second collapse as in mercury. For the case of $S = 10^6$ m^{-1}, a bubble in water disintegrates after the fifth collapse during the bouncing motion after the violent collapse although a bubble in mercury is shape stable because the bubble expansion in water is much larger and the subsequent bubble collapse is much stronger than in mercury.

The dotted line in Fig. 3(a) is the calculated result for the density of water with the other physical quantities being the same as those of mercury. The difference between the dotted line and the dash-dotted line for water in Fig. 3(a) is due to the difference in the surface tension and the saturated vapor pressure. The effect of surface tension on the radius-time curve is shown in Fig. 3(b). In water, much more vapor diffuses into the bubble during the bubble expansion due to the much higher saturated vapor pressure compared to mercury, which also causes more expansion of a bubble [Figs. 3(c) and 3(d)]. On the other hand, the effect of the diffusion of gas across the bubble wall is negligible because the change in the number of helium (or xenon) atoms inside a bubble is less than 1% according to the present numerical simulations.

The maximum temperature inside a bubble at the bubble collapse in water is lower than that in mercury due to the much larger amount of vapor [Figs. 4(a) and 4(b)]. Water vapor has

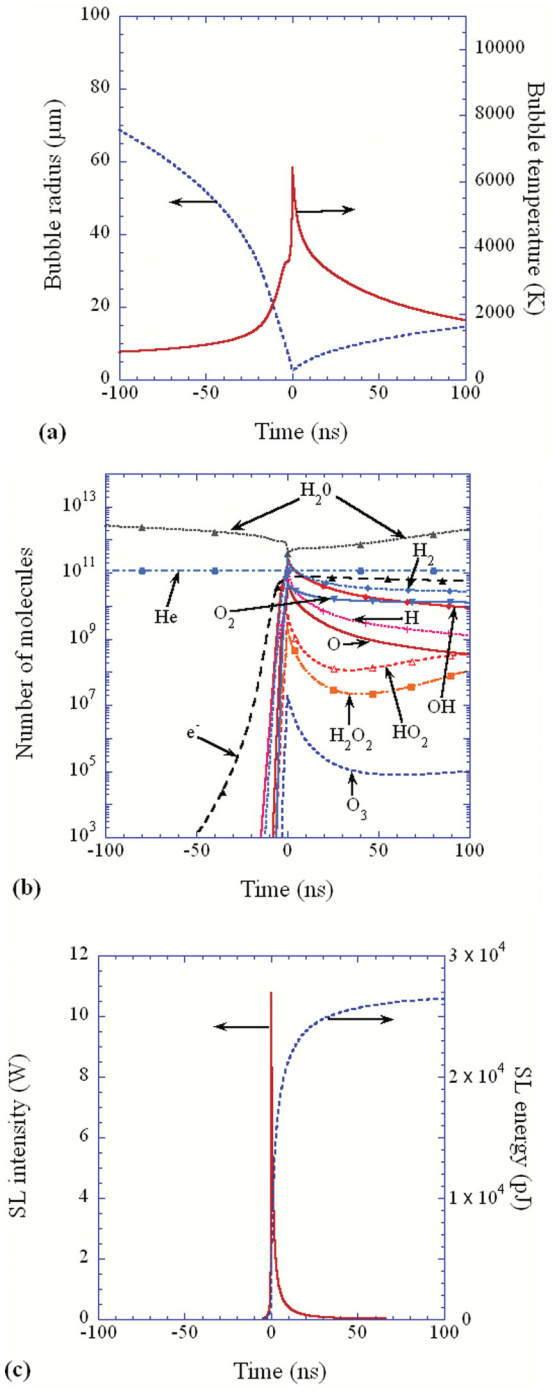

FIG. 4. (Color online) The result of the numerical simulation for a He bubble in water. The other conditions are the same as those in Fig. 2.

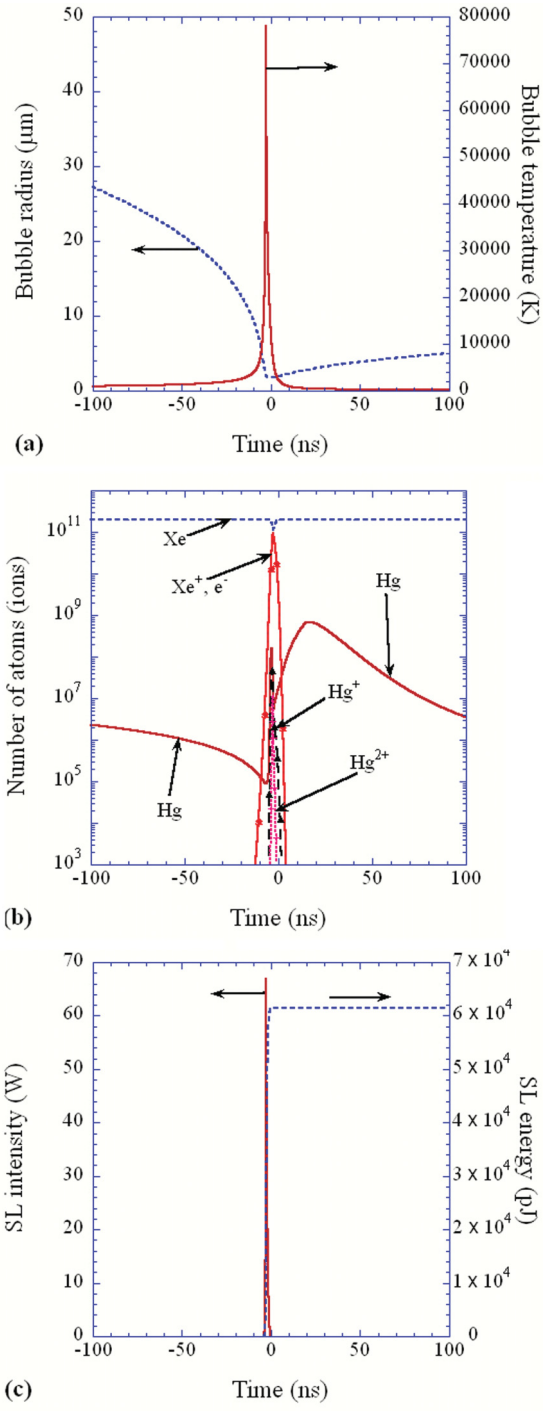

FIG. 5. (Color online) The result of the numerical simulation for a Xe bubble in mercury. The other conditions are the same as those in Figs. 2 and 4.

a larger molar heat than that of monoatomic gases such as He, Xe, and Hg. In addition, water vapor is dissociated inside a heated bubble and consumes an appreciable fraction of the thermal energy inside a bubble. The SL intensity, however, is higher than that in mercury because the number of free electrons inside a bubble in water is much larger than that in mercury [Figs. 2(b) and 4(b)]. This is because the ionization potentials of water vapor and its dissociation products are lower than that of He (Table IV).

Next, the collapse of Xe bubbles is discussed. The maximum temperature inside a Xe bubble in mercury is much higher than that inside a He bubble due to lower thermal conductivity which results in a smaller amount of thermal conduction from the heated bubble interior into the surrounding liquid [Figs. 2(a) and 5(a)]. Under the present condition, the maximum temperature inside a Xe bubble is as high as 78 000 K. It should be noted that in SBSL in water the maximum temperature inside a bubble is usually less than

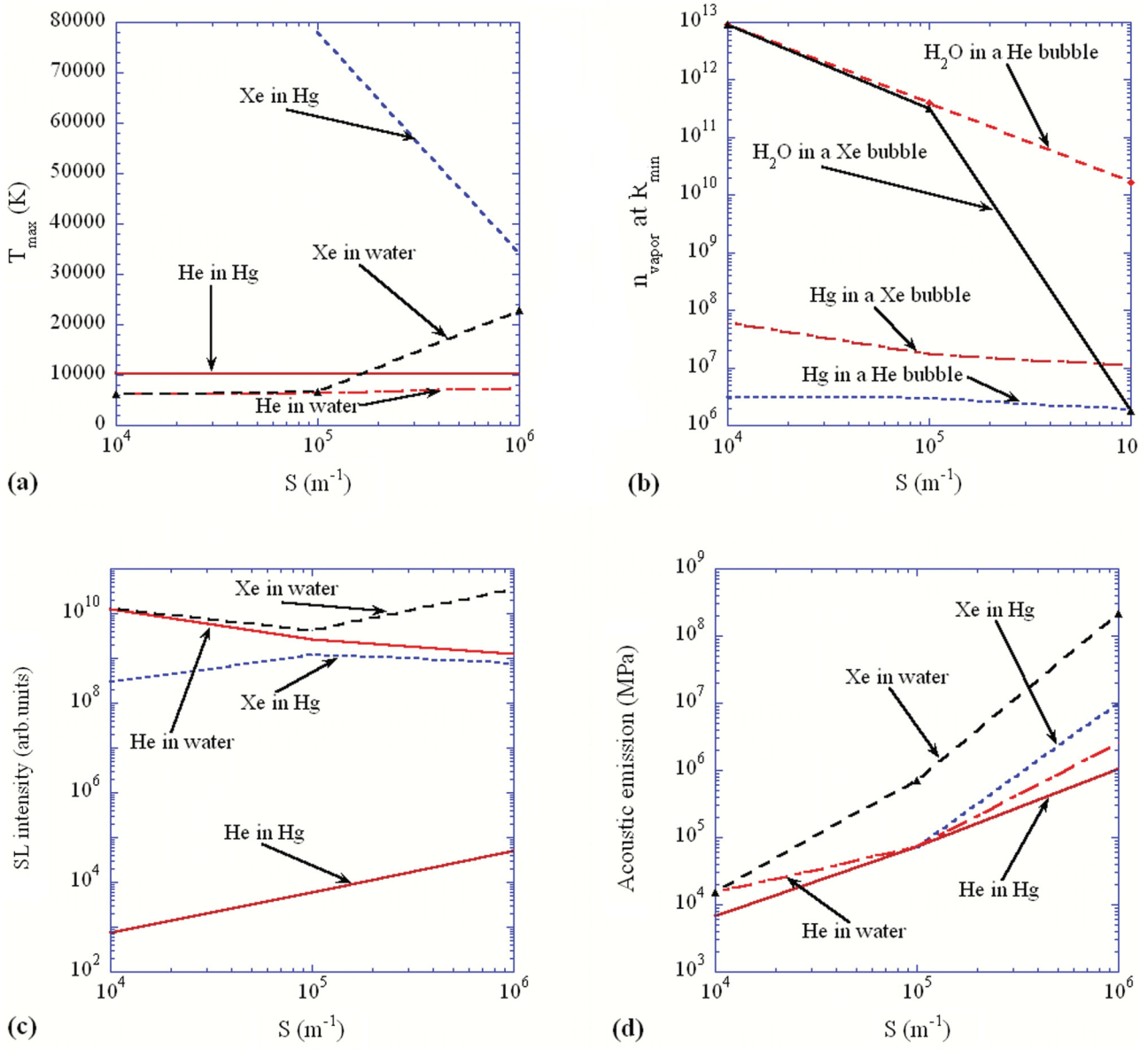

FIG. 6. (Color online) The summary of the results of numerical simulations as a function of S ($R_0 = 10$ μm). (a) The maximum bubble temperature. (b) The number of vapor molecules inside a bubble at the end of the violent bubble collapse. (c) The SL intensity [S (proportional to the number of bubbles) times the SL energy in picojoules per bubble collapse]. (d) The maximum pressure in the liquid due to shock waves radiated by bubbles.

20 000 K [28,47]. Due to the very high temperature inside a Xe bubble as well as the much lower ionization potential compared to He, the number of free electrons inside a Xe bubble is a few orders of magnitude larger than that in a He bubble [Figs. 2(b) and 5(b)]. The ionization potential of Xe is reduced by about 44% inside a bubble and the maximum degree of ionization is as high as 0.46, while it is only 10^{-4} for He. It may be consistent with the experimentally determined degree of ionization of 0.19 for a Xe bubble at the bubble temperature of 10 000 K in dehydrated phosphoric acid [45]. As a result, the SL intensity from a Xe bubble is four orders of magnitude higher than that from a He bubble [Figs. 2(c) and 5(c)]. Thus it is concluded that Xe is much more suitable than He for the monitoring of the cavitation activity by the SL light emission.

The results of the numerical simulations are summarized in Fig. 6. The maximum temperature inside a Xe bubble is higher than that inside a He bubble both in mercury and in water due to lower thermal conductivity [Fig. 6(a)]. The maximum bubble temperature in mercury is higher than that in water both for He and Xe bubbles due to a much smaller amount of vapor inside a bubble [Fig. 6(b)]. The maximum temperature inside a Xe bubble in mercury decreases as S increases because the bubble expansion becomes less [Fig. 1(b)] and the subsequent bubble collapse becomes milder. On the other hand, the maximum temperature inside a Xe bubble in water increases as S increases above 10^5 m^{-1} because the amount of water vapor, which cools the bubble, substantially decreases [Fig. 6(b)]. In contrast, for a He bubble in water, the maximum temperature

does not significantly increase as S increases above 10^5 m^{-1}. For a He bubble in mercury, the maximum temperature does not increase as S decreases in contrast with a Xe bubble. The both tendencies are due to the much higher thermal conductivity of He than that of Xe (Table III) as much of the thermal energy is lost by the thermal conduction for a He bubble.

The amount of mercury vapor inside a Xe bubble is larger than that in a He bubble because the minimum bubble radius is larger due to higher bubble temperature and pressure [Fig. 6(b)]. The drop in the amount of water vapor at $S = 10^6$ m^{-1} for Xe bubbles in water compared to that for He bubbles is due to the dissociation of water vapor caused by the much higher temperature inside a bubble [Fig. 6(a)].

The SL intensity from Xe bubbles is higher than that from He bubbles both in mercury and water [Fig. 6(c)] due to higher temperature and lower ionization potential. The SL intensity in water is higher than that in mercury both from He and Xe bubbles. Jarman [51] and Golubnichii *et al.* [52] showed that the SL intensity increases as σ^2/p_v^* of the liquid increases, where σ is the surface tension and p_v^* is the saturated vapor pressure. According to their hypothesis, the SL intensity in mercury should be much higher than that in water. However, the results of the present numerical simulations have indicated that it is not always the case.

The SL intensity from He bubbles in water decreases as S increases because the amount of water vapor decreases due to less expansion of the bubble [Fig. 6(b)]. Water vapor is the source of free electrons and intensifies SL. Thus, as the amount of water vapor inside a bubble decreases, the SL intensity decreases.

For Xe bubbles in water, the SL intensity has a minimum around $S \sim 10^5$ m^{-1}. On one hand, the amount of water vapor inside a bubble decreases as S increases [Fig. 6(b)]; on the other hand, the temperature inside a bubble as well as the number of bubbles increases [Fig. 6(a)]. Due to these contrary tendencies for SL, there is a minimum at around $S \sim 10^5$ m^{-1}.

For He bubbles in mercury, the SL intensity monotonously increases as S increases because the number of bubbles increases. The maximum pressure in the liquid due to shock waves emitted from bubbles monotonously increases as S increases for all the cases because the number of bubbles increases [Fig. 6(d)]. Thus, for He bubbles in mercury, the SL intensity is well correlated with the maximum pressure due to shock waves (Fig. 7). It suggests that SL may be a good indicator of the physical effect of acoustic cavitation for He bubbles in mercury. On the other hand, for Xe bubbles in water, the SL intensity is not at all correlated with the maximum pressure due to shock waves because the SL intensity depends on S in a complex way; there are many factors which determine the SL intensity such as the amount of water vapor inside a bubble, the maximum temperature inside a bubble and the number of bubbles.

According to the present numerical simulations, the maximum SL intensity from a Xe bubble in water is as high as 200 W for $R_0 = 10$ μm and $S = 10^4$ m^{-1}. It is comparable to the experimentally reported value of 100 W from a Xe bubble in phosphoric acid driven by a strong acoustic pulse [53].

Finally, the diffusion-limited vapor transport model is discussed. According to the numerical simulations by Storey and Szeri [54], the mass transport of vapor across the bubble

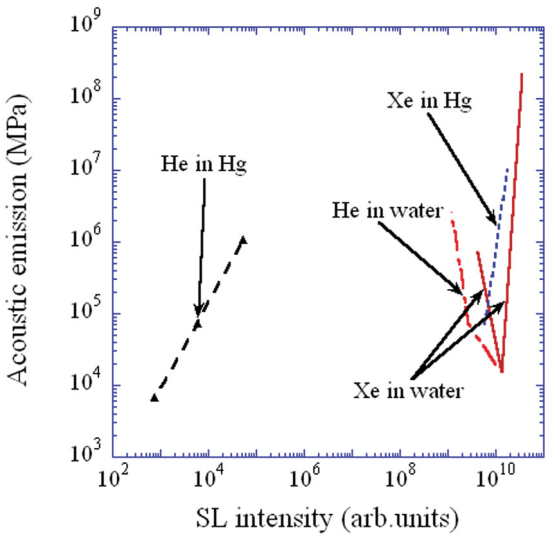

FIG. 7. (Color online) The relationship between the SL intensity and the maximum pressure in the liquid due to shock waves radiated by bubbles according to the numerical simulations ($R_0 = 10$ μm).

wall is limited by the slow diffusion of vapor inside a bubble. In the present model [Eqs. (8)–(10)], however, the mass transport of vapor is assumed to be limited by a nonequilibrium phase change rather than the diffusion. Toegel and Lohse [55] have constructed a simple model of diffusion-limited vapor transport. In the present study, we also have performed numerical simulations using the model of Toegel and Lohse [55] instead of Eqs. (8)–(10). According to Toegel and Lohse [55] the rate of evaporation ($\dot{m}$) is calculated by the following equation:

$$\dot{m} = D_{\mathrm{vapor}} \frac{c_{\mathrm{vapor},\,0} - c_{\mathrm{vapor}}}{l_{\mathrm{vapor}}}, \tag{18}$$

where D_{vapor} is the diffusion constant of vapor in the gas phase, $c_{\mathrm{vapor},\,0}$ is the saturated vapor concentration at the liquid temperature near the bubble wall, c_{vapor} is the vapor concentration inside a bubble, and l_{vapor} is the diffusive boundary layer thickness of vapor. The diffusion constant (D_{vapor}) is estimated by the equation given in Ref. [56]. The saturated vapor concentration at the liquid temperature at the bubble wall ($c_{\mathrm{vapor},\,0}$) is calculated by the following equation:

$$c_{\mathrm{vapor},\,0} = \frac{c_{\mathrm{vapor+gas}}\, p_v^*}{p}, \tag{19}$$

where $c_{\mathrm{vapor+gas}}$ is the total concentration of gases and vapor inside a bubble, p_v^* is the saturated vapor pressure at the liquid temperature near the bubble wall, and p is the pressure inside a bubble [Eq. (4)]. The diffusive boundary layer thickness of vapor (l_{vapor}) is estimated by the following equation:

$$l_{\mathrm{vapor}} = \min\left(\sqrt{\frac{R D_{\mathrm{vapor}}}{|\dot{R}|}}, \frac{R}{\pi}\right). \tag{20}$$

Here, we recall the result of numerical simulations by Storey and Szeri [29] that a gas mixture is mildly segregated inside a collapsing bubble due to the temperature and pressure gradients within the bubble. The lighter gas molecules are driven to the bubble center and the heavier gas molecules

TABLE V. The comparison between the results of numerical simulations based on the present model and the diffusion-limited vapor transport model for xenon bubbles in mercury ($S = 10^5$ m^{-1}, $R_0 = 10$ μm).

	Present model	Diffusion-limited
T_{max}	78 000 K	78 000 K
R_{min}	1.75 μm	1.75 μm
n_{Hg} at R_{min}	1.8×10^7	5.6×10^9
n_{Xe} at R_{min}	2.0×10^{11}	2.0×10^{11}
SL	6.1×10^{-8} J	6.5×10^{-8} J
Acoustic emission	7.1×10^4 MPa	5.4×10^4 MPa

are driven to the bubble wall by the thermal and pressure diffusion. In a helium bubble in mercury, helium atoms are driven to the bubble center and mercury (Hg) atoms are driven to the bubble wall because the molecular weight of helium (MW = 4) is much smaller than that of mercury (MW = 201). Thus the concentration of mercury vapor near the bubble wall is higher than that near the bubble center during the bubble collapse. It contradicts Eq. (18) because the numerical simulations have indicated that $c_{vapor,0} < c_{vapor}$ during the bubble collapse. Thus, this model cannot be used for a helium bubble in mercury.

On the other hand, the molecular (atomic) weights of xenon (MW = 131) and mercury (MW = 201) are not so different. In this case, mixture segregation may not be significant and Eq. (18) can be used. In Table V, the comparison between the results of the numerical simulations based on the present model and the diffusion-limited vapor transport model is shown. There is not a significant difference between them with regard to the SL and acoustic intensities.

In Table VI, the results for xenon bubbles in water are listed for the two models. For the diffusion-limited vapor transport model, however, the number of water vapor molecules inside a bubble is three orders of magnitude larger than that of xenon atoms. It means that Eq. (18) no longer holds because Eq. (18) means a strong accumulation of Xe atoms near the bubble wall or a large pressure drop near the bubble wall as $c_{vapor,0} \ll c_{vapor}$. The strong accumulation of Xe atoms near the bubble wall means that the concentration of Xe atoms near the bubble wall should be a few orders of magnitude larger than that of water vapor, although the total number of Xe atoms is three orders of magnitude smaller than that of water molecules. It is not realistic because the results of numerical simulations by Stroey and Szeri [29] suggest that the mixture segregation is much milder. On the other hand, if there is a pressure drop near the bubble wall, the diffusion of water vapor is strongly accelerated by the pressure difference and Eq. (18) cannot be used. Thus the diffusion-limited vapor transport model [Eq. (18)] is not self-consistent in this case. The same problem also arises for helium bubbles in water.

TABLE VI. The comparison between the results of numerical simulations based on the present model and the diffusion-limited vapor transport model for xenon bubbles in water ($S = 10^5$ m^{-1}, $R_0 = 10$ μm).

	Present model	Diffusion limited
T_{max}	6,700 K	4500 K
R_{min}	2.76 μm	16.3 μm
n_{H_2O} at R_{min}	3.2×10^{11}	2.9×10^{14}
n_{Xe} at R_{min}	1.2×10^{11}	1.2×10^{11}
SL	4.3×10^{-8} J	3.5×10^{-7} J
Acoustic emission	7.2×10^5 MPa	1.7×10^5 MPa

In conclusion, the diffusion-limited vapor transport model [Eq. (18)] only works for xenon bubbles in mercury. The results are not significantly different from those based on the present model with regard to the SL and acoustic intensities from bubbles. Thus the conclusions based on the present model are at least qualitatively correct.

IV. CONCLUSION

Numerical simulations of pulsation and light emission (SL) of He or Xe bubbles in mercury and water have been performed under the conditions of the experiment by Futakawa *et al.* [15]. The SL intensity from Xe bubbles is much higher than that from He bubbles due to lower ionization potential and higher bubble temperature due to lower thermal conductivity. It suggests that SL from Xe may be more suitable than that from He as an indicator of cavitation damage in mercury. On the other hand, SL is not an indicator of cavitation damage in water because the amount of water vapor inside a bubble influences the SL intensity in a complex way through the amount of free electrons and the maximum temperature inside a bubble.

ACKNOWLEDGMENTS

The authors would like to thank M. Futakawa, S. Hasegawa, and M. Ida of J-PARC center in the Japan Atomic Energy Agency for valuable comments.

[1] B. T. M. Willis and C. J. Carlile, *Experimental Neutron Scattering* (Oxford University Press, Oxford, 2009).
[2] A. Furrer, J. Mesot, and T. Strassle, *Neutron Scattering in Condensed Matter Physics* (World Scientific, Hackensack, NJ, 2009).
[3] J. S. Higgins and H. C. Benoit, *Polymers and Neutron Scattering* (Oxford University Press, Oxford, 1996).
[4] M. Bee, *Quasielastic Neutron Scattering* (Adam Hilger, Bristol and Philadelphia, 1988).
[5] S. W. Lovesey, *Theory of Neutron Scattering from Condensed Matter*, Vols. 1, 2 (Oxford University Press, Oxford, 1984).
[6] A. Taylor, M. Dunne, S. Bennington, S. Ansell, I. Gardner, P. Norreys, T. Broome, D. Findlay, and R. Nelmes, Science **315**, 1092 (2007).
[7] G. S. Bauer, J. Nucl. Mater. **398**, 19 (2010).
[8] M. Futakawa, H. Kogawa, S. Hasegawa, Y. Ikeda, B. Riemer, M. Wendel, J. Haines, G. Bauer, T. Naoe, K. Okita, A. Fujiwara, Y. Matsumoto, and N. Tanaka, J. Nucl. Mater. **377**, 182 (2008).

[9] S. J. Pawel and L. K. Mansur, J. Nucl. Mater. **398**, 180 (2010).
[10] D. A. McClintock, P. D. Ferguson, and L. K. Mansur, J. Nucl. Mater. **398**, 73 (2010).
[11] N. J. Manzi, P. V. Chitnis, R. G. Holt, R. A. Roy, R. O. Cleveland, B. Riemer, and M. Wendel, J. Acoust. Soc. Am. **127**, 2231 (2010).
[12] B. Riemer, J. Haines, M. Wendel, G. Bauer, M. Futakawa, S. Hasegawa, and H. Kogawa, J. Nucl. Mater. **377**, 162 (2008).
[13] M. Futakawa, T. Naoe, C.-C. Tsai, H. Kogawa, S. Ishikura, Y. Ikeda, H. Soyama, and H. Date, J. Nucl. Mater. **343**, 70 (2005).
[14] M. Futakawa, K. Kikuchi, H. Conrad, and H. Stechemesser, Nucl. Instrum. Methods Phys. Res., Sect. A **439**, 1 (2000).
[15] M. Futakawa, T. Naoe, and M. Kawai, in *Nonlinear Acoustics—Fundamentals and Applications: 18th International Symposium on Nonlinear Acoustics (ISNA 18)*, AIP Conf. Proc. No. 1022, edited by B. O. Enflo, C. M. Hedberg, and L. Kari (AIP, New York, 2008), p. 197.
[16] M. Ida, T. Naoe, and M. Futakawa, Nucl. Instrum. Methods Phys. Res., Sect. A **600**, 367 (2009).
[17] M. Ida, T. Naoe, and M. Futakawa, Phys. Rev. E **75**, 046304 (2007).
[18] M. Ida, T. Naoe, and M. Futakawa, Phys. Rev. E **76**, 046309 (2007).
[19] H. Kuttruff, Acustica **12**, 230 (1962).
[20] R. T. Smith, G. M. B. Webber, F. R. Young, and R. W. B. Stephens, Adv. Phys. **16**, 515 (1967).
[21] M. Ida, K. Haga, H. Kogawa, T. Naoe, and M. Futakawa, J. Phys. Soc. Jpn. **79**, 044401 (2010).
[22] K. Yasui, A. Towata, T. Tuziuti, T. Kozuka, and K. Kato, J. Acoust. Soc. Am. **130**, 3233 (2011).
[23] K. Yasui, T. Tuziuti, J. Lee, T. Kozuka, A. Towata, and Y. Iida, J. Chem. Phys. **128**, 184705 (2008).
[24] K. Yasui, Phys. Rev. E **56**, 6750 (1997).
[25] K. Yasui, T. Tuziuti, M. Sivakumar, and Y. Iida, J. Chem. Phys. **122**, 224706 (2005).
[26] K. Yasui, Y. Iida, T. Tuziuti, T. Kozuka, and A. Towata, Phys. Rev. E **77**, 016609 (2008).
[27] K. Yasui, J. Lee, T. Tuziuti, A. Towata, T. Kozuka, and Y. Iida, J. Acoust. Soc. Am. **126**, 973 (2009).
[28] K. Yasui, Phys. Rev. E **64**, 016310 (2001).
[29] B. D. Storey and A. J. Szeri, J. Fluid Mech. **396**, 203 (1999).
[30] *CRC Handbook of Chemistry and Physics*, edited by D. R. Lide (CRC Press, Boca Raton, FL, 1994).
[31] K. Yasui, T. Tuziuti, J. Lee, T. Kozuka, A. Towata, and Y. Iida, Ultrason. Sonochem. **17**, 460 (2010).
[32] K. Yasui, J. Phys. Soc. Jpn. **65**, 2830 (1996).
[33] R. C. Reid, J. M. Prausnitz, and T. K. Sherwood, *The Properties of Gases and Liquids* (McGraw-Hill, New York, 1977).
[34] M. L. Huber, A. Laesecke, and D. G. Friend, Ind. Eng. Chem. Res. **45**, 7351 (2006).
[35] J. Kestin and J. H. Whitelaw, ASME J. Eng. Power **88**, 82 (1966).
[36] Y. S. Touloukian, R. W. Powell, C. Y. Ho, and P. G. Klemens, in *Thermal Conductivity, Metallic Elements and Alloys*, Thermophysical Properties of Matter, Vol. 1 (IFI/Plenum, New York-Washington, DC, 1970), p. 221.
[37] Y. S. Touloukian, P. E. Liley, and S. C. Saxena, *Thermal Conductivity, Nonmetallic Liquids and Gases*, Thermophysical Properties of Matter, Vol. 3 (IFI/Plenum, New York-Washington, DC, 1970).
[38] K. Yasui, Ultrasonics **40**, 643 (2002).
[39] M. Matsumoto, Fluid Phase Equilib. **125**, 195 (1996).
[40] K. Yasui, J. Acoust. Soc. Am. **112**, 1405 (2002).
[41] A. Eller and H. G. Flynn, J. Acoust. Soc. Am. **37**, 493 (1965).
[42] T. G. Leighton, *The Acoustic Bubble* (Academic Press, London, 1994).
[43] G. B. Zimmerman and R. M. More, J. Quant. Spectrosc. Radiat. Transfer **23**, 517 (1980).
[44] R. M. More, J. Quant. Spectrosc. Radiat. Transfer **27**, 345 (1982).
[45] S. Khalid, B. Kappus, K. Weninger, and S. Putterman, Phys. Rev. Lett. **108**, 104302 (2012).
[46] K. Yasui, T. Tuziuti, M. Sivakumar, and Y. Iida, Appl. Spectrosc. Rev. **39**, 399 (2004).
[47] M. P. Brenner, S. Hilgenfeldt, and D. Lohse, Rev. Mod. Phys. **74**, 425 (2002).
[48] S. Hilgenfeldt, D. Lohse, and M. P. Brenner, Phys. Fluids **8**, 2808 (1996).
[49] F. R. Young, *Sonoluminescence* (CRC Press, Boca Raton, FL, 2005).
[50] B. P. Barber, R. A. Hiller, R. Lofstedt, S. J. Putterman, and K. R. Weninger, Phys. Rep. **281**, 65 (1997).
[51] P. Jarman, Proc. Phys. Soc. **73**, 628 (1959).
[52] P. I. Golubnichii, V. D. Goncharov, and K. V. Protopopov, Sov. Phys. Acoust. **16**, 115 (1970).
[53] B. Kappus, S. Khalid, and S. Putterman, Phys. Rev. E **83**, 056304 (2011).
[54] B. D. Storey and A. J. Szeri, Proc. R. Soc. London, Ser. A **456**, 1685 (2000).
[55] R. Toegel and D. Lohse, J. Chem. Phys. **118**, 1863 (2003).
[56] R. C. Reid, J. M. Prausnitz, and B. E. Poling, in *The Properties of Gases and Liquids*, 4th ed. (McGraw-Hill, New York, 1988), pp. 581–583 and Appendix B.